Published April 11, 2019

Original Research

Core Ideas

- 3D MRI relaxation time maps reflect water mobility in root, rhizosphere, and soil.
- 3D NCT water content maps of the same plant complement relaxation time maps.
- The relaxation time T_1 decreases from soil to root, whereas water content increases.
- Parameters together indicate modification of rhizosphere pore space by gel phase.
- The zone of reduced T_1 corresponds to the zone remaining dry after rewetting.

Combination of Magnetic Resonance Imaging and Neutron Computed Tomography for Three-Dimensional Rhizosphere Imaging

S. Haber-Pohlmeier,* C. Tötzke, E. Lehmann, N. Kardjilov, A. Pohlmeier, and S.E. Oswald

In situ investigations of the rhizosphere require high-resolution imaging techniques, which allow a look into the optically opaque soil compartment. We present the novel combination of magnetic resonance imaging (MRI) and neutron computed tomography (NCT) to achieve synergistic information such as water mobility in terms of three-dimensional (3D) relaxation time maps and total water content maps. Besides a stationary MRI scanner for relaxation time mapping, we used a transportable MRI system on site in the NCT facility to capture rhizosphere properties before desiccation and after subsequent rewetting. First, we addressed two questions using water-filled test capillaries between 0.1 and 5 mm: which root diameters can still be detected by both methods, and to what extent are defined interfaces blurred by these imaging techniques? Going to real root system architecture, we demonstrated the sensitivity of the transportable MRI device by co-registration with NCT and additional validation using X-ray computed tomography. Under saturated conditions, we observed for the rhizosphere in situ a zone with shorter T1 relaxation time across a distance of about 1 mm that was not caused by reduced water content, as proven by successive NCT measurements. We conclude that the effective pore size in the pore network had changed, induced by a gel phase. After rewetting, NCT images showed a dry zone persisting while the MRI intensity inside the root increased considerably, indicating water uptake from the surrounding bulk soil through the still hydrophobic rhizosphere. Overall, combining NCT and MRI allows a more detailed analysis of the rhizosphere's functioning.

Abbreviations: 3D, three-dimensional; DAS, day after seeding; FOV, field of view; MRI, magnetic resonance imaging; NCT, neutron computed tomography; NMR, nuclear magnetic resonance; RARE, rapid acquisition with relaxation enhancement; XCT, X-ray computed tomography.

S. Haber-Pohlmeier, Institute of Technical and Macromolecular Chemistry, RWTH Aachen Univ., Worringerweg 2, D-52074 Aachen, Germany; C. Tötzke and S.E. Oswald, Institute of Environmental Science and Geography, Univ. Potsdam, 14476 Potsdam, Germany; E. Lehmann, Paul Scherrer Institute, 5232 Villigen, Switzerland; N. Kardjilov, Helmholtz Center Berlin for Materials and Energy, 14109 Berlin, Germany; A. Pohlmeier, IBG-3, Research Center Jülich, Wilhelm Johnen Str., D-52425 Jülich, Germany. *Corresponding author (haber-pohlmeier@itmc.rwth-aachen.de).

Received 3 Sept. 2018.
Accepted 28 Jan. 2019.
Supplemental material online.

Citation: Haber-Pohlmeier, S., C. Tötzke, E. Lehmann, N. Kardjilov, A. Pohlmeier, and S.E. Oswald. 2019. Combination of magnetic resonance imaging and neutron computed tomography for three-dimensional rhizosphere imaging. Vadose Zone J. 18:180166. doi:10.2136/vzj2018.09.0166

The interface between bulk soil and root, termed the *rhizosphere*, is a zone of intense activity that controls water and solute uptake. It is essentially a soil compartment that is modified actively and dynamically in many ways by root activities and associated microorganisms (Carminati and Vetterlein, 2013; Gregory, 2006; Hinsinger et al., 2009; Vetterlein et al., 2013; Whalley et al., 2005). Most knowledge about the chemical, biochemical, and microbial composition of the rhizosphere and their changes due to nutrient uptake comes from optical observations and sampling using two-dimensional rhizotrons (Gregory and Hinsinger, 1999). In contrast, less is known about its water transport properties and its impact on water fluxes, for example, root water uptake. Generally, water moves along potential gradients in the soil–plant–atmosphere continuum, which has led to the expectation of constant moisture or even depletion of water around active roots in soils (Gardner, 1960). However, experimental results are contradictory in the sense that some studies have reported decreasing water content toward roots (MacFall et al., 1990; Segal et al., 2008; Young, 1995), other studies have mentioned increasing water content toward roots (Carminati et al., 2010; Moradi et al., 2011; Nishiyama, 2005; Tumlinson et al., 2008), or both in different parts (Esser et al., 2010). Depending on the desiccation and rewetting

history, the water content gradient from the rhizosphere to the bulk soil can also reverse for a certain time period (Carminati et al., 2010). A plausible explanation is the exudation of mucilage by the root. This hydrogel increases the water holding capacity during drying but at the same time is responsible for the reverse behavior after rewetting. The interpretation of the rhizosphere properties so far relies on the application of one single imaging method. Since each method possesses its individual strength, a method combination promises added value and will contribute to an increased understanding of rhizosphere behavior. More specifically, we intended to combine water content mapping by NCT with relaxation time mapping and relaxation weighted imaging by MRI to conclude on pore space modifications that influence water mobility and manifest in changed relaxation times.

Neutrons are strongly attenuated by hydrogenous compounds such as water. Therefore, neutron tomography is a suitable tool to map the 3D water distribution in soil with high accuracy. Because root tissue is mainly composed of water, neutrons provide good contrast between roots and soil, especially at low soil water content. The high spatial and temporal resolution of two-dimensional neutron radiography permits the visualization of changes at the soil–root interface without disturbance of the hydraulic gradients. The spatial resolution commonly used in plant root experiments ranges from 50 to 200 μm depending on imaging conditions and sample size. Neutron radiography was tested decades ago for application to soil–root systems, e.g., to study the germination and root growth of corn (*Zea mays* L.) (Couchat et al., 1980). Later studies, with higher level technical facilities coming into place, observed inhibited water uptake by soybean [*Glycine max* (L.) Merr.] roots due to the presence of vanadium in the soil (Furukawa et al., 1999). In the last decade, neutron imaging components have improved substantially, and more investigators have started to study root–soil systems either by two-dimensional neutron radiography or 3D neutron tomography (Moradi et al., 2011; Oswald et al., 2015). One achievement of this development is unprecedented high-resolution tomography of several plant root systems in sandy soil. Hence it became possible to resolve the rhizosphere water content, which can be higher or lower than in the bulk soil depending on the desiccation and rewetting history (Moradi et al., 2011). In addition, neutrons can distinguish between different isotopes and provide high contrast between, e.g., hydrogen (high beam attenuation) and deuterium (low beam attenuation). Experiments using deuterated "heavy" water as a contrast agent allow observation of water uptake in the root system and the acquisition of quantitative information about the water dynamics in the plants (Matsushima et al., 2009) and recently also in three dimensions in soil (Tötzke et al., 2017). However, a limitation of this method results from the high attenuation of neutrons by H_2O. Plant sample sizes are necessarily small (about 3 cm in diameter) and the soil should not be too wet (water content $\theta < 0.25$ cm^3 cm^{-3}) to ensure sufficient beam transmission. The achievable resolution is 50 μm for typical samples of 30-mm diameter and 100-mm height. Furthermore, neutron imaging experiments can only be performed at a few large-scale facilities where the neutron beam is provided by an atomic reactor (e.g., BER II research reactor located at Helmholtz Center Berlin in Germany) or a spallation source (e.g., SINQ at the Paul Scherrer Institute, Villigen, Switzerland). This limits the access to neutron imaging experiments and beam time allocation considerably.

Magnetic resonance imaging, best known from medicine, is nowadays well established in material science (Blümich, 2000; Callaghan, 1990; McRobbie et al., 2007). It uses the spatially resolved nuclear magnetic resonance (NMR) signal, frequently a spin echo, which is encoded in three spatial directions by switching magnetic field gradients in combination with radiofrequency pulses. After excitation, the signal decays by two different relaxation processes, longitudinal (T_1) and transverse (T_2) relaxation. Together with the proton density, both relaxation times control the signal intensity in each voxel in combination with experimental parameters such as the echo time t_E, the repetition time t_R, or, if applicable, a preparation time. By adjusting these experimental parameters, the signal can be made sensitive to proton density, i.e., to water content, or to T_2 and T_1 relaxation. Relaxation times in soil material and the rhizosphere are often fast and show a broad distribution in contrast to humans or rodents. As a result, water content imaging with MRI is challenging and often difficult to achieve quantitatively. In contrast, NCT has the great advantage of high sensitivity to the total, static proton density and is thus an ideal method for quantitatively determining the water content. Therefore, we combined NCT and MRI to be sure to get the total water content with high accuracy.

On the other hand, MRI offers the possibility of obtaining relaxation-time weighted images as well as relaxation time maps that allow conclusions to be drawn about local water mobility. In the context of NMR, water mobility means the molecular mobility based on rotational and translational diffusion. These motions create fluctuating local magnetic fields responsible for the relaxation processes. In porous media, the local mobility of water can be restricted by adsorption at solid–liquid interfaces, confinement in narrow structures, incorporation in gels, or exchange among bulk, surface, and polymer phases (Belton, 1997; Brownstein and Tarr, 1977, 1979; Kimmich, 2012). Consequently, short relaxation times occur for water molecules residing in small pores (Kleinberg et al., 1994), in films at low water contents (Haber-Pohlmeier et al., 2014), or if water is incorporated in gels (Bertasa et al., 2018; Brax et al., 2017). When mucilage from chia seed (*Salvia hispanica* L.) is mixed with soil, the situation becomes more complex. Brax et al. (2018) proposed a so-called *gel effect* characterized by accelerated bulk and surface relaxation even at constant pore size and water content. In a recent work, van Veelen et al. (2018) reported about relaxation time mapping at high field using the transverse relaxation time instead of the longitudinal relaxation.

As already mentioned above, we measured water content independently by NCT and combined it with relaxation time mapping. In this way, the individual strengths of both methods, MRI and NCT, were combined for in situ imaging of the rhizosphere. In preparatory experiments we first dealt with two questions: which

root diameters are still visible and to what extent is an interface possibly blurred by imaging techniques? These questions were addressed using two different test phantoms composed of water-filled capillaries in wet sand with variable diameters down to 0.1 mm. Another prerequisite for method combination is the co-registration. It comprises the exact matching of root system images from different sources, with different resolutions and orientations, and is demonstrated by an example imaging study of the root system architecture by MRI, NCT, and, in addition, by X-ray CT. Subsequently, we investigated the root system and rhizosphere of a broad bean (*Vicia faba* L.) grown in sandy soil under two conditions: before desiccation and after rewetting. We recorded the T_1 relaxation time maps with a stationary 1.5 T MRI system at full saturation because T_1 is proportional to the pore size only under these conditions. After transportation to the neutron facility, a mobile MRI scanner allowed relaxation time weighted MRI in parallel to complement the NCT measurements.

Methods and Materials

Transportable Magnetic Resonance Imaging Scanner, 0.6 Tesla

The transportable MRI system was purchased from Magritek Ltd. It consists of multiple stacked rings of permanent magnets of a SmCo alloy arranged in a Halbach array so that the magnetic field B_0 of 0.57 T (24.2 MHz for the hydrogen atom) points perpendicular to the main axis of the magnet (Fig. 1a) (Danieli et al., 2010). Adjustable shim magnets are placed between the fixed building blocks and, together with the gradient system, homogeneity of <6 ppm for a working volume of 40 by 40 by 40 mm is achievable. The gradient system with a maximum strength of 300 mT m^{-1} is water cooled and placed inside the magnet bore with a diameter of 10 cm. The vertical magnet orientation is used for plant imaging, but the magnet unit could also be rotated to horizontal orientation without the problems of cryogen liquids.

Radiofrequency solenoid coils of two sizes are available: one with an inner diameter of 60 mm and a length of 80 mm resulting in a usable axial field of view (FOV) with a length of 60 mm, and a smaller one designed for higher resolution and signal/noise ratio with a diameter of 30 mm and an identical axial FOV. The MRI magnet unit has a total mass of about 150 kg. For transport in a car or on rough floors, it is mounted on a special vibration-damped trolley made entirely of non-magnetic stainless steel (Fig. 1b). The system is operated by a KEA^2 spectrometer (Magritek Ltd.) possessing three gradient channels and one radiofrequency channel with a maximum power of 350 W and three separate linear amplifiers (AE Techron) for the gradient system. All equipment fits into the back of a small van (Fig. 1c). The measurement campaigns were performed in large experimental halls of the neutron facilities with a high level of electromagnetic noise. Therefore, it was necessary to reduce the noise level by grounding and wrapping the electronics and cables with conductive tissue acting as a Faraday cage. The shimming was controlled and optimized by the Prospa software (Magritek) applying DC currents to the different gradient coils. The final preparatory step was the determination of a 90° pulse length and the integral T_1 and T_2 relaxation times of the samples using a saturation recovery and Carr, Purcell, Meiboom, Gill (CPMG) pulse sequence, respectively.

To image the root system architecture and water in the surrounding soil material, a 3D rapid acquisition with relaxation enhancement (RARE) sequence was chosen. This sequence is most suitable for low-field measurements because it allows short measurement times in the range of 1.5 h to be achieved with an accumulation of eight scans. We used the following sequence parameters: echo time t_E = 6.8 ms, repetition time t_R = 10 s, matrix sizes = 128 by 128 by (128 or 64) corresponding to the voxel resolutions given in Supplemental Table S1. When using a RARE sequence, it is important to check that the T_2 decay after one echo train is sufficiently long so that the last echo still has enough signal intensity. The corresponding spatial resolutions before zero filling are summarized in Supplemental Table S1. The images were obtained by 3D inverse Fast Fourier transformation after zero filling by a factor of 2 and filtering with a 3D sine bell function to reduce Gibbs ringing artifacts and interpolate the acquired raw data matrix (Blümich, 2000). It should

Fig. 1. The transportable Magritek magnetic resonance imaging (MRI) tomograph built of permanent magnets: (a) schematic drawing of one ring-shaped Halbach array with main building block magnets and shim magnets (gray)—several of such rings are stacked to form the entire magnet; (b) the tomograph is mounted on a vibration-damped trolley; and (c) the instrumentation including magnet, spectrometer, chiller, and amplifiers can be transported easily in a small van.

be noted here that the RARE sequence is inherently T_2 weighted and consequently most sensitive to image a root system possessing long T_2 relaxation times. Furthermore, the fraction of soil water with long T_2 is detectable, too. The root system was segmented by thresholding and subsequent region growing, which extracts connected pixels of similar intensity.

Stationary Magnetic Resonance Imaging Scanner, 1.5 Tesla

For the T_1 mapping in three dimensions, we used a Varian 1.5 T split-coil magnet equipped with a 0.3 T m^{-1} gradient system and a vertical 60-mm solenoid radiofrequency coil. The system is operated by a Varian spectrometer and VNMRJ 3.0 software (Agilent Technologies). The T_1 maps were calculated from a series of single echo multislice (SEMS) images with inversion recovery preparation, using inversion times t_{inv} of 0.1, 0.2, 0.4, 0.8, and 1.6 s plus a reference image with no inversion recovery preparation. For details, see Haber-Pohlmeier et al. (2017). Here only the most important sequence parameters are given as t_R = 8 s, t_E = 4 ms, FOV = 60 by 60 by 66 mm, matrix size = 256 by 256, and 30 slices of 2-mm thickness with a gap of 0.2 mm, which corresponds to a voxel resolution of 234 µm by 234 µm by 2.2 mm. We used the stationary scanner for T_1 mapping because the transportable system allows it only in single slices so that covering the entire 3D space would result in extremely long total measuring times. This needs further development and will be subject of a following study.

Neutron Computed Tomography

These experiments were performed at the neutron facilities of the Helmholtz Center Berlin for Energy and Materials in Berlin, Germany, and the Paul Scherrer Institute in Villigen, Switzerland. Neutron measurements of test samples and the broad bean plant (Sample B14) shown in Fig. 2 to 4 were performed at the BER II research reactor of the Helmholtz Center Berlin using the cold neutron imaging instrument CONRAD II (Kardjilov et al., 2015). The collimation ratio L/D used at the imaging instrument was 170. The detector system was equipped with a 200-µm-thick ^{6}LiZnS:Ag scintillator and a 16-bit CCD camera (Andor DW-436N-BV) with 2048 by 2048 pixels in combination with a Nikon photo lens (AF-S NIKKOR 50 mm 1:1.4G). Five hundred radiographs with an exposure time of 7 s each and a resolution of 50 µm per pixel were taken while the sample was rotated stepwise through an angular range of 180°. The acquisition time for the entire scan was 80 min. Projection images were corrected by flat-field and dark-field images.

The neutron experiments with another broad bean plant (Sample B12J) shown in Fig. 5 were performed at the Paul Scherrer Institute using the imaging station NEUTRA, which is supplied with thermal neutrons by the spallation source SINQ (Lehmann et al., 2001). Samples were imaged at the middle measuring position of the instrument, where the collimation ratio L/D is 350 using a 100-µm-thick ^{6}LiZnS scintillator as the detector screen. The absorption images formed on the scintillator screen were captured by a Neo sCMOS camera equipped with a Nikon photo lens (AF-S NIKKOR 50 mm 1:1.4G) at a resolution of 97 µm per pixel. For the tomographic measurement, 500 radiographic projections were taken while the sample was rotated stepwise through an angular range of 360°. Exposure time of a single radiograph was 5 s. Including read-out times, the total acquisition time for a tomogram was about 2 h. Dark-field and flat-field corrections of the neutron absorption images were applied to eliminate the dark current signal and the inhomogeneities of the beam profile, respectively. Fluctuations in beam intensity were normalized using the intensity values of a sample free region of the detector screen as reference. White spots in

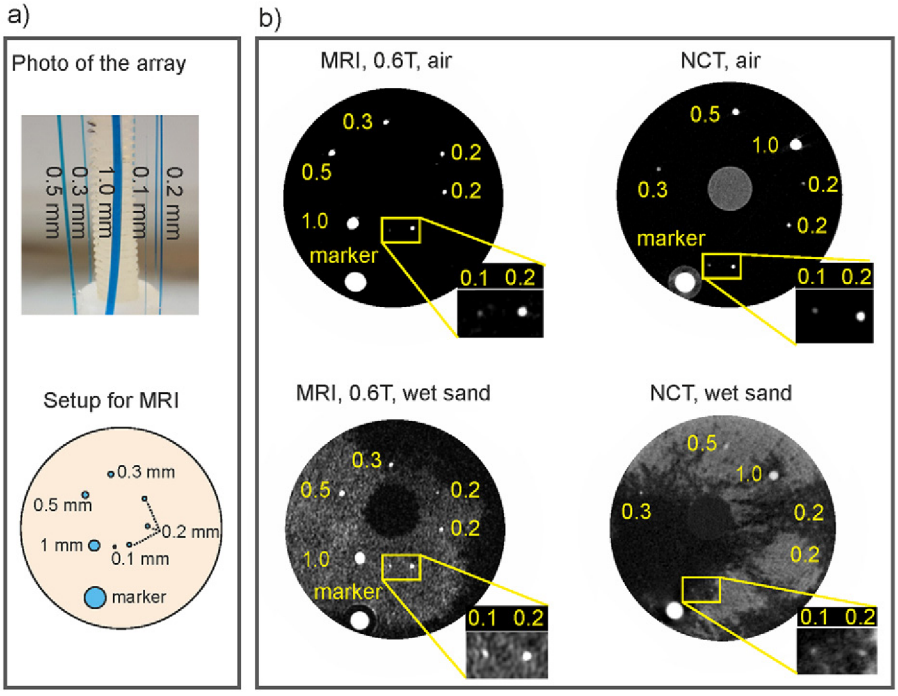

Fig. 2. (a) Setup of test Phantom 1 for the magnetic resonance imaging (MRI) scans: seven plastic tubes were filled with stained water (tube diameters in millimeters are noted inside the photo); (b) axial slices in the air region (top row) and wet sand region (bottom row) of the phantom measured by MRI at 0.6 T and neutron computed tomography (NCT), with yellow numbers indicating the diameters of the tubes. Please note that the internal arrangement of the capillaries for NCT differed from that of MRI. The cut-outs show close-ups of the region with the 0.1- and 0.2-mm tubes.

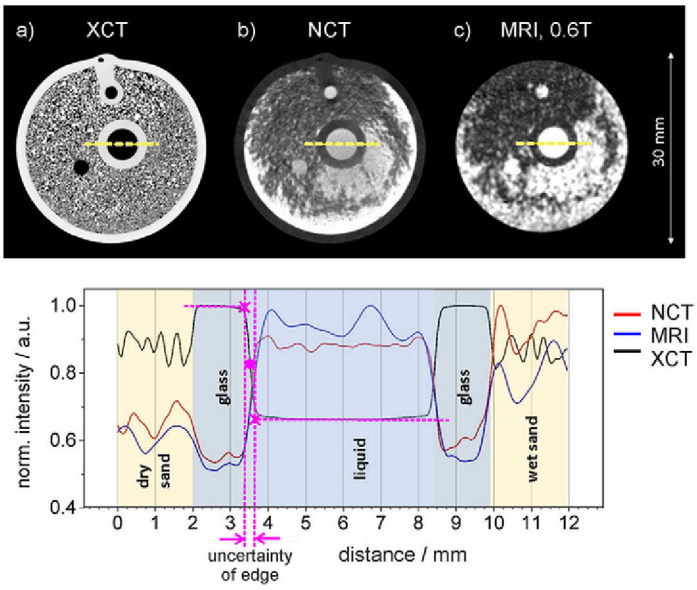

Fig. 3. Top: Selected slices from (a) X-ray computed tomography (XCT), (b) neutron computed tomography (NCT) (measured at Helmholtz Center Berlin), and (c) magnetic resonance imaging (MRI) images of test Phantom 2 at 0.6 T with built-in tubes of different diameters. Bottom: intensity profiles along the yellow lines in the top images. The vertical dotted lines indicate the uncertainty range of an edge for the example of the XCT profile. It is defined as the distance between the intersection points (magenta crosses) of the average intensities in the liquid and glass with the tangent through the inflection point (magenta dot).

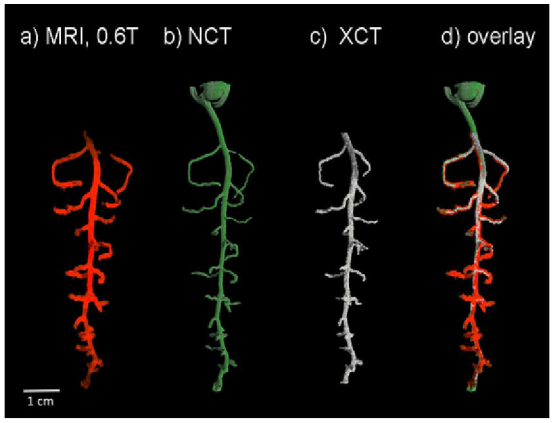

Fig. 4. Co-registration of the root system architecture (Sample B14) extracted from the complementary three-dimensional data sets: (a) magnetic resonance imaging (MRI) at 0.6 T monitored on day after seeding (DAS) 21 at the Helmholtz Center Berlin, (b) neutron computed tomography (NCT) monitored on DAS 21 at the Helmholtz Center Berlin, (c) X-ray computed tomography (XCT) monitored on DAS 19 at the Helmholtz Center Berlin, and (d) overlaid root systems demonstrating the good agreement of root structures measured by the individual techniques.

the radiograms caused by impinging gamma photons were removed using the "remove outlier" filter of the software ImageJ.

X-ray Computed Tomography

X-ray computed tomography measurements were performed at the Helmholtz Center Berlin using a laboratory μCT scanner with a cone beam geometry. The major components of the scanner are a 150 kV micro-focus X-ray source (Type L8121-03, Hamamatsu Photonics), a sample manipulation stage, and a flat panel detector (Type C7942SK-05, Hamamatsu Photonics) with 2316 by 2316 pixels. The acceleration voltage and current of the X-ray source was set to 90 kV and 111 μA, respectively. The detector pixel size was 50 by 50 μm. The source object distance was 225 mm and the source detector distance 330 mm, resulting in an image resolution of 34 μm per pixel and a corresponding FOV of 77.8 by 77.8 mm. Eleven hundred radiographic projections were recorded through an angular range of 360°. Three frames with 0.6-s exposure time were taken at each angular step and a median image calculated to improve the statistics of the projection image. The total acquisition time per tomogram was 63 min. Tomograms were reconstructed from all neutron and XCT images and rendered in three dimensions using the software tools Octopus (Inside Matters) and VGstudio Max (Volume Graphics).

Co-registration

The co-registration of the 3D image datasets comprised following steps: matching the FOV, aspect ratio, resolution, and 3D orientation of two or more volume datasets from different imaging methods. We used a manual approach to keep full control during the image registration procedure. After initial coarse alignment, the pixel size and FOV of the MRI and XCT datasets were matched to parameters of the NCT images. The scaled volumes were subsequently aligned so that features of the root system and an additional marker tube matched optimally. The Supplemental Material contains a detailed description of the individual alignment steps during the co-registration. It involved scaling, re-slicing, rotation, and translation operations applied on the image stacks performed using the software ImageJ (https://imagej.net/Fiji).

Phantom 1

Phantom 1 consisted of an arrangement of seven water-filled polyethylene terephthalate glycol (PETG) capillaries (Paradigm Optics) with inner diameters of 0.1, 0.2, 0.3, 0.5, and 1 mm. All capillaries were filled with a Brilliant Blue solution under vacuum and sealed immediately after filling. For reasons of stability, the tubes were fixed on a polyethylene holder for MRI (Fig. 2a) and on a polytetrafluorethylene (PTFE) holder for NCT. The assemblies were set into a glass cuvette with 27-mm inner diameter, which was subsequently filled with dry sand (FH31, Quarzwerke Frechen). It should be noted that the phantom was decomposed after MRI measurements and recomposed on the PTFE holder to provide sufficient beam transmission during NCT, which explains the different arrangements of the tubes in the MRI and NCT images. Additionally, a marker tube filled with 0.5 mM Gd-DTPA in 80:20 D_2O/H_2O (w/w) was fixed inside the glass cuvette made of boron-free quartz glass (HSQ300, Heraeus) to avoid strong neutron beam attenuation by boron. The phantom was first scanned in dry sand and second in a partially saturated state at a water content of $\theta = 0.17$ cm^3 cm^{-3}.

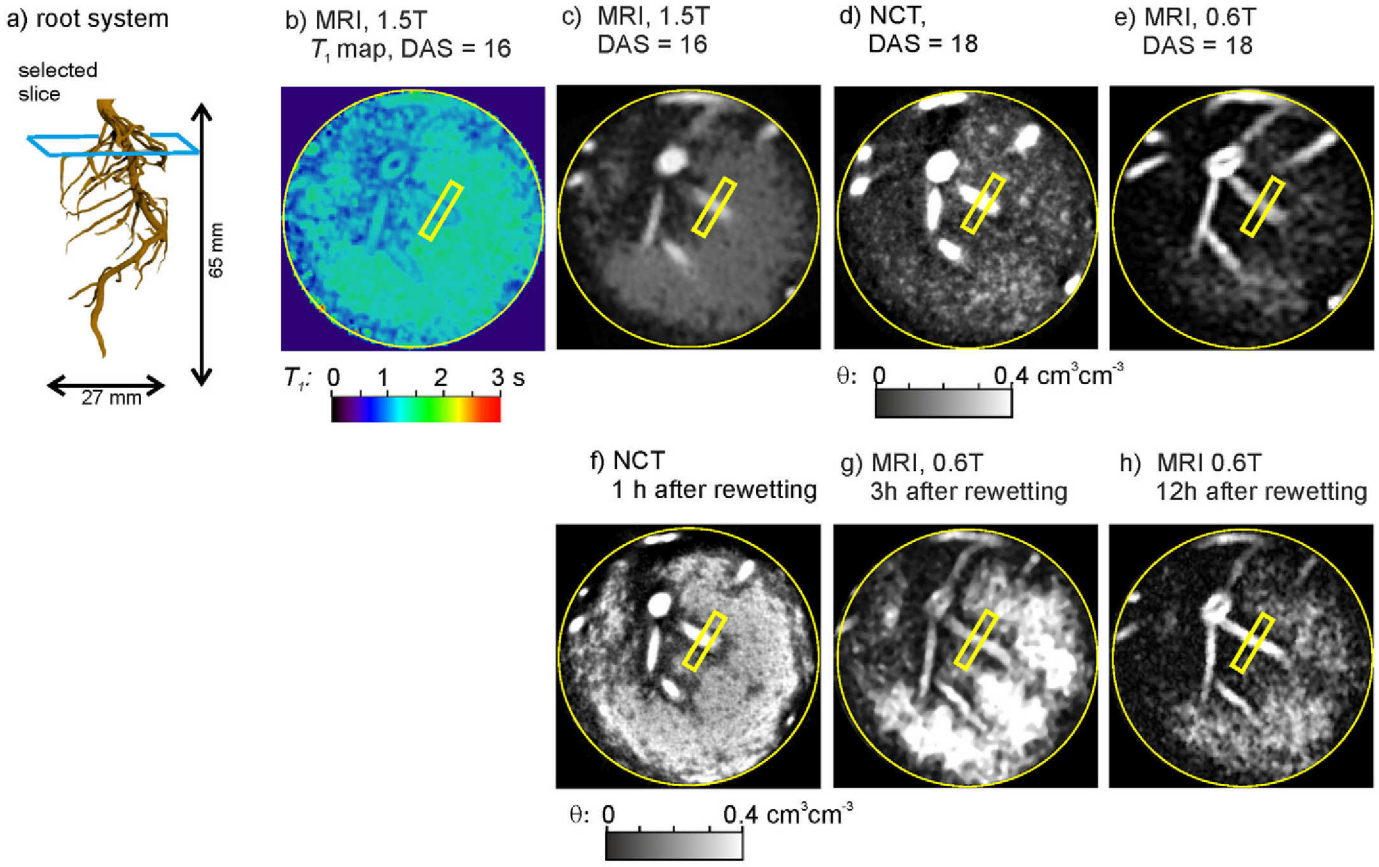

Fig. 5. (a) Root system of broad bean (Sample B12J) grown in sand imaged with neutron computed tomography (NCT), the wireframe indicates the position of the selected slice out of three-dimensional data sets for further detailed analysis; (b) map of relaxation time T_1 on day after seeding (DAS) 16; (c) magnetic resonance imaging (MRI) image (reference image of the inversion time t_{inv} series) on DAS 16 with an in-plane physical resolution of 0.23 by 0.23 mm and slice thickness of 2.2 mm; (d) NCT image on DAS 18 with an isotropic resolution of 0.097 mm and calibrated to water content (θ) in sand; (e) MRI image on DAS 18 measured with the transportable scanner at 0.6 T with a nominal spatial resolution (without zero filling) of 0.31 by 0.31 mm and slice thickness of 1.09 mm (note that the roots appear different in the MRI and NCT images due to the larger slice thicknesses); (f–h) the state of the selected slice on DAS 24 after rewetting, at resolutions identical to (c–e): (f) NCT image 1 h after rewetting and calibrated to water content in sand and MRI images at 0.6 T after (g) 3 h and (h) 12 h. The image intensities were normalized on a reference tube (not shown). All images were co-registered using ImageJ after matching the individual resolutions to those of the NCT images.

Phantom 2

A second phantom was constructed because the wall material of Phantom 1 was visible by NCT due to its high content of hydrogen atoms. Phantom 2 consisted of stiff glass tubes with diameters ranging from 2.0 to 2.6 to 5 mm and wall thicknesses of 1, 0.01, and 1.5, respectively. Our aim was to check the detectability of hard edges by both methods, to cross-check these structures by XCT, and to test the co-registration procedure. The tubes were filled with a mixture of 80:20 D_2O/H_2O (w/w) and placed in a cylindrical glass cuvette of 2.7-cm inner diameter and 10-cm length containing FH31 sand, with a porous plate at the bottom. The sand was saturated with water from the bottom to a volumetric water content of $\theta = 0.22$ cm^3 cm^{-3}.

Plant Growth and Timeline

Broad bean seeds (Freudenberger Feldsaaten) were pre-germinated on day after seeding (DAS) 0 for 2 d in tap water and subsequently planted directly in the measuring cuvettes in wet FH31 sand. We used the same cuvettes as described above for the test phantoms. To restrict undesired evaporation, the surface was covered with a 0.5-cm layer of coarse sand. The beans grew for about 2 wk while being irrigated regularly to maintain an average water content of $\theta = 0.30$ cm^3 cm^{-3}. A 14/10 h day/night cycle of illumination was set at a temperature of 23°C, a relative humidity of 60%, and a photosynthetically active photon flux density of 450 μmol m^{-2} s^{-1}. Eight plants were grown for each measurement campaign, from which two were selected for detailed investigations termed in the following B14 and B12J for the campaigns at Helmholtz Center Berlin and Paul Scherrer Institute, respectively. Sample B12J was additionally investigated by MRI at 1.5 T in a fully saturated state to determine the relaxation time maps immediately before transport to the Paul Scherrer Institute. After transport and between the single scans, the plant remained in a climate chamber at 23°C and a humidity of 60% in the neutron hall at the Paul Scherrer Institute, and the water content was monitored frequently by weighing. At a water content of 0.04 cm^3 cm^{-3} on DAS 24, the plant was irrigated to a volumetric water content of 0.2 cm^3 cm^{-3} and immediately scanned. Soil domain dimensions,

bulk densities, and volumetric water contents at the time of scanning as well as scan days are summarized in Supplemental Table S1.

Results and Discussion

Phantom 1 consisted of water-filled capillaries with known diameters ranging from 0.1 to 1 mm and was designed to prove the suitability of NCT and MRI to detect fine root structures in wet sand. Figure 2b shows axial slices at two different positions: in the air region (Fig. 2b top row) and in partially saturated sand (Fig. 2b, bottom row). Additionally, we present profiles through the 0.1- and 0.2-mm-wide tubes in the Supplemental Material. We could show that both methods detect capillaries with diameters $\geq$0.1 mm even in partially wet sand. This means that roots with 0.2-mm diameter are clearly visible even at higher water contents where the contrast between root and surrounding soil is less pronounced. Please note that the smallest detectable diameter of 0.1 mm is below the resolution of 0.16 mm used for the 0.6 T MRI scanner. It confirms the results of Metzner et al. (2015), who presented a sub-voxel resolution for root system imaging. The reason is the high contrast between water-filled structures like roots and their environment. Thus, even voxels that are only partially filled with roots show the presence of such structures.

An engineered sample with known geometry, Phantom 2, was used to evaluate edge blurring by NCT and MRI after co-registration (Fig. 3). In this case we also included XCT as the method with the highest resolution and providing good contrast between compartments of different density, i.e., between glass and water (Peth, 2010). In the XCT image (top row, left) the structures formed by solid materials, i.e., glass walls and soil particles can be unambiguously identified, whereas the H_2O–D_2O mixture inside the tubes yields almost no signal as expected. The thickness of the glass wall of the largest tube (1.5 mm) is clearly reproduced in all images, whereas the thin glass wall (10 μm) of the 2.6-mm-wide tube is resolved by none of the imaging techniques. In contrast to XCT, water distribution in the sand material is visible by NCT and MRI. By normalization of the voxel intensities in the sand compartment on the water content in the thick marker tube, we obtained an average water content in the given slice of 0.21 cm^3 cm^{-3} for NCT, which agrees well with the gravimetrically determined water content of 0.22 cm^3 cm^{-3}. The diameters of the tubes have been determined in all images from the positions of the inflection points of the profiles. We obtained for the 5-mm-wide tube a diameter of 4.8 mm by all methods. Accordingly, the inner diameter of the 2.0-mm thick-walled tube was determined as 2.0 mm by XCT and NCT and 2.1 mm by MRI. For the 2.6-mm thin-walled capillary, NCT, XCT, and MRI provided diameters of 2.7, 2.8, and 2.6 mm, respectively. The errors for the diameters result from the inaccuracy of the edge position, i.e., the edge blurring. It is determined by the intersection of the tangent at the inflection point with the average intensity of the liquid and glass compartment. By way of example, this procedure is shown for the XCT profile in the bottom panel of Fig. 3. The numerical values are ±0.13, ±0.2, and ±0.3 mm for XCT, NCT, and MRI, respectively. Later, we used these errors for the inaccuracy of the position of the root surface that is, the onset of the rhizosphere.

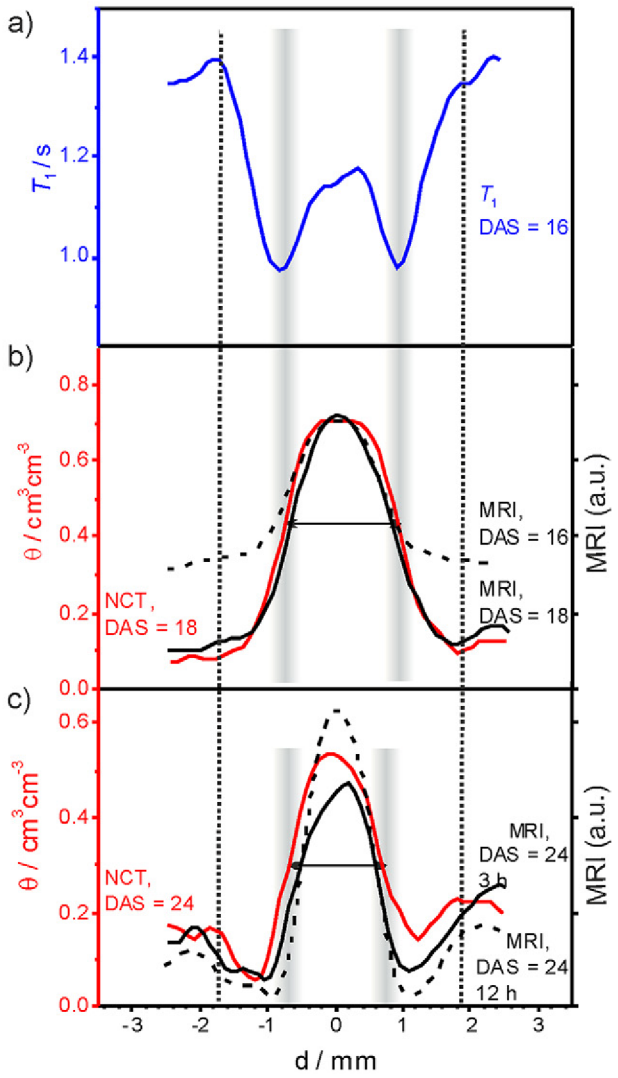

Fig. 6. Plots of 5-mm-long profiles across the lateral root indicated by the yellow rectangles in Fig. 5: (a) T_1 relaxation time profile at saturation on day after seeding (DAS) 16, monitored with the 1.5 T scanner; (b) calibrated neutron computed tomography (NCT) intensities on DAS 18 (red curve), magnetic resonance imaging (MRI) at 1.5 T on DAS 16 (black dashed curve), and MRI at 0.6 T on DAS 18 (black full curve); (c) profiles after rewetting on DAS 24, with calibrated NCT intensities (red curve), MRI at 0.6 T 3 h after rewetting (black full curve), and MRI at 0.6 T 12 h after rewetting (black dashed curve). The gray bars indicate the position and uncertainty range of the root outer surface. The distance scale is shifted so that the origin is in the center of the root. The vertical dotted lines indicate the approximate outer boundary of the rhizosphere on both sides of the root. This is defined as the range where the T_1 relaxation time reaches the typical value for saturated bulk sand.

Co-registration

Because we compare water content maps from NCT scans with relaxation times maps or relaxation weighted images from MRI, it is important to know that the datasets are not shifted

against each other. This is achieved through co-registration. For this purpose, we scanned the root system of a broad bean in wet sand with NCT, MRI at 0.6 T, and XCT as the method with the highest resolution. We present the result of the co-registration procedure as perspective views rendered from the complementary image data sets in Fig. 4 and, for better visualization, by a corresponding video sequence in Supplemental Video S1. The root systems extracted from MRI (Fig. 4a), NCT (Fig. 4b), and XCT (Fig. 4c) are displayed together as an overlay in Fig. 4d. Root structures match almost perfectly, emphasizing the precision in the alignment of the complementary 3D imaging data. Moreover, all roots that were detected by XCT are also visible by NCT and the 0.6 T MRI scanner. Only one gap in the second lateral root appears in the MRI and NCT images, possibly caused by root damage or decay. Please note that some lateral roots in the XCT image appear markedly shorter than in the NCT and MRI images. The reason is the time difference of 2 d between the XCT and NCT measurements, a period in which these roots grew by about 6 mm. The successful co-registration of the data is the proof that the water content maps from NCT and relaxation time maps of MRI are not shifted against each other. This is necessary for interpreting the data together.

Rhizosphere Analysis

Based on root activity, the presence of root hairs, and associated microorganisms, changes in the pore space properties of the rhizosphere compared with the bulk soil should be expected. These will become manifest in changed NMR relaxation times and changed water content visible in MRI relaxation time maps and NCT images, respectively. The top row in Fig. 5 shows NCT and MRI images of a broad bean plant in sand at two points in time: first, measured at the stationary 1.5 T MRI scanner on DAS 16, and second, measured 2 d later by NCT and the transportable 0.6 T MRI without irrigation in the meantime. The 3D root system image (Fig. 5a, NCT dataset) indicates the position of one axial slice, selected for subsequent detailed analysis. To emphasize that the selected slice is not just an isolated case, the corresponding images of other slices can be found in the Supplemental Material and in Haber-Pohlmeier et al. (2018). Figure 5b shows the T_1 relaxation time maps for the initial state at a water content of $\theta = 0.34$ cm^3 cm^{-3} on DAS 16. Remarkable are the zones with accelerated relaxation surrounding the taproot as well as the lateral roots. Due to large plant cells filled with water, the roots appeared bright with a good contrast to the surrounding soil in the MRI and NCT images (Fig. 5c–5e). The water is distributed uniformly in the greater part of the slice. The average water content is obtained by integration over the entire soil domain of the NCT image as $\theta = 0.13$ cm^3 cm^{-3}, which is in good agreement with the gravimetrically obtained value of $\theta = 0.14$ cm^3 cm^{-3} after the NCT scan. Note that most lateral roots are inclined with respect to the axial plane (Fig. 5a). Because the slice thickness of the MRI image is larger than for NCT, inclined roots appear longer in the MRI image (Fig. 5e) than in the NCT image (Fig. 5d).

For a more detailed analysis of the rhizosphere in terms of relaxation times and water content, we extracted profiles along a 1-mm section through a lateral root, indicated by the yellow rectangles in Fig. 5. The profiles extend across the root, the rhizosphere, and the adjacent bulk soil on both sides and are plotted in Fig. 6a and 6b. On DAS 16, the MRI profile (black dashed curve in Fig. 6b) shows constant intensity in the water-saturated soil and an increase of signal intensity inside the root caused by the higher water content of the root tissue. Two days later on DAS 18, the shape of the local water content profile as retrieved from the calibrated NCT image (red curve in Fig. 6b) is similar inside the root but differs for the adjacent soil region. The root surface at the inflection points of the NCT and MRI profiles on DAS 18 can be located at $d = -0.8$ and 0.8 mm, resulting in a root diameter of 1.6 ± 0.3 mm (double arrow), taking into account the results of Phantom 2. Beyond the root surface, the water content decreased from $\theta = 0.4$ cm^3 cm^{-3} across a distance of about 1 mm before reaching the value of $\theta = 0.15$ cm^3 cm^{-3} in the bulk soil. The maximum water content at the root surface is even slightly higher than the total porosity of the chosen sand material, calculated from the bulk density as 0.39 cm^3 cm^{-3}. However, our results agree very well with the observations for different beans of Nishiyama (2005), who determined increased water content across a distance of 0.5 mm. Similar results were obtained for corn using NCT (Tumlinson et al., 2008). Later, Carminati et al. (2010) and Moradi et al. (2011) reported an increased water content of 0.4 cm^3 cm^{-3} at the root surface of chick pea (*Cicer arietinum* L.) and lupine (*Lupinus* L.). They postulated an enhanced water holding capacity in the rhizosphere induced by the exudation of mucilage.

So far, we have discussed the results on the water content gradient in the rhizosphere obtained with high accuracy by NCT. The combination with MRI images of the same plant allows a further characterization of the rhizosphere by analysis of T_1 relaxation time maps. The T_1 profile (full blue curve in Fig. 6a) shows a symmetric shape starting with a value of 1.4 s characteristic for bulk sand (Duschl et al., 2016). From there, the relaxation time decreases by about 30% to 0.9 s at the root surface. Inside the root, T_1 increases to about 1.15 s in the center and decreases again to 0.9 s at the opposite root surface.

To understand the relaxation time behavior in the rhizosphere, we discuss possible combinations of relaxation time and water content gradients looking from the bulk soil to the root surface as illustrated in Fig. 7. We assume the Brownstein–Tarr model for relaxation in porous media, which separates the relaxation process into contributions of bulk and surface relaxation (Barrie, 2000; Brownstein and Tarr, 1977). In Fig. 7a, no changes in T_1 and θ are expected because the pore size and filling factor do not change. In Fig. 7b, the pore size increases from soil to rhizosphere, and T_1 and water content would also increase. This scenario could appear as a consequence of particle shifting due to alternating shrinking and swelling of the roots. Figure 7c concerns a reduced pore size and porosity in the rhizosphere due to soil compaction. Under saturated

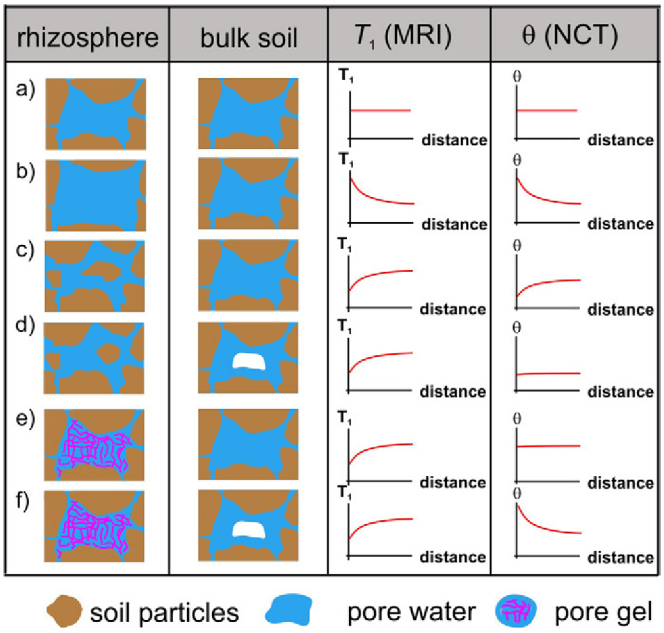

Fig. 7. Different scenarios for the filling of the pore space from rhizosphere to bulk soil and the impact on relaxation and neutron computed tomography (NCT) water content profiles. Relaxation times T_1 and water content θ are plotted as a function of the distance from the root surface. Note that T_1 profiles in (d) and (f) depend on the degree of desaturation.

conditions, T_1 and water content will decrease from soil to root, while under unsaturated conditions (Fig. 7d) the water content remains approximately constant at a level corresponding to the enhanced packing density in the rhizosphere. In Fig. 7e and 7f, we consider an additional hydrogel phase in the rhizosphere. Without any change in the pore size, the relaxation time decreases from soil to rhizosphere while the water content remains constant (Fig. 7e). With decreasing saturation of the bulk soil, an increased water content in the rhizosphere due to the water attraction by the hydrophilic hydrogel would be observed as shown in Fig. 7f. Considering the different scenarios clearly shows that our combined results are best described by Fig. 7f.

While the effect of mucilage collected from roots on NMR relaxation times has not yet been investigated, some studies have described the impact of mucilage from chia seeds, synthetic hydrogels, and biofilms. Our data agree very well with the data of Brax et al. (2018). They investigated chia seed gel in wet sand mimicking the rhizosphere. Relaxation times T_1 and T_2 were accelerated due to enhanced contributions of surface and bulk relaxation. A year before, Buchmann and Schaumann (2017) discussed an increase in relaxation times when synthetic hydrogel is added to clay-containing soil material. They related this shift to an increase in the pore size due to swelling of the polymers. Van Veelen et al. (2018) used T_2 mapping measured at high field for the investigation of packed and loose hydrated chia seeds in quartz sand or Nafion with subsequent degradation. They reported an increase in the relaxation time T_2 of hydrated chia seeds in sand packing during decomposition, when the mucilage concentration decreased. These examples show that the shift in the relaxation time to higher or lower values is very sensitive and depends on the composition of the soil material, the hydraulic history, and the type of hydrogel. All these factors might impact the relaxation mechanism and therefore relaxation times. Another type of gel is biofilm produced by microbial activity. Also in such systems relaxation times are significantly shorter, as mentioned by Codd et al. (2011) for a model bead pack with different parts of biofouling. Against this background, it cannot yet be clarified whether shifts in the relaxation times are due to microbial biofilm development, mucilage exudation, or both. On the other hand, it is certain that the measured short relaxation times are due to a gel phase (see Fig. 7).

An additional effect on the relaxation times may result from the penetration of root hairs into the pore space. First of all, neither NCT nor MRI are able to resolve root hairs within the resolution given by the cuvette diameter of 3 cm and maximum number of points of 1024 and 256, respectively. Consequently, to resolve root hairs cuvettes with significantly smaller dimensions should be used, as reported by Keyes et al. (2013). However, keep in mind that going to small dimensions means a higher restriction of natural growth conditions. A penetration of root hairs into the pore space would not lead to higher water content as discussed by Carminati et al. (2010) and is in contrast to our results. Anyway, mean free pathways for water diffusion would be decreased, leading to accelerated relaxation. This open question could be addressed by comparison of natural and bald genotypes.

Rewetting

After a drying period, during which the water content dropped to 0.04 $cm^3\ cm^{-3}$, the plant was rewetted on DAS 24 to an average water content of 0.20 $cm^3\ cm^{-3}$ and immediately scanned by NCT and MRI using the transportable setup on site. Directly after rewetting, dry zones remained around the roots, whereas the water content in the bulk soil appeared relatively high (see Fig. 5f). The corresponding relaxation time weighted MRI image (Fig. 5g) shows similar results, i.e., high signal intensity in the bulk soil and pronounced dark zones around the root. Twelve hours later, the intensity inside the roots has increased considerably at the expense of a lower intensity in the bulk soil domain (Fig. 5h). The corresponding profiles in Fig. 6c, drawn through the same lateral root as analyzed before, show the behavior more quantitatively. The most important point is that the decrease in water content coincides with the region of reduced T_1 relaxation time (see Fig. 6a). This is a direct proof that the rhizosphere possesses different hydraulic properties than the bulk soil. It corresponds directly to the presence of the gel phase indicated by T_1. The MRI profiles on DAS 24 after 3 and 12 h show the same trend in the rhizosphere. Our data are consistent with water content data of Carminati et al. (2010), who showed pronounced dry zones around roots after drought stress and rewetting. This was attributed to different hydraulic properties of the rhizosphere (Carminati et al., 2010; Moradi et al., 2011). In addition, the intensity within the root clearly increased during this time by about 30%, while at the

same time that of the bulk soil decreased (Fig. 6c, dashed curve). It is not possible to quantitatively translate these intensity changes into water content changes, but qualitatively they indicate water uptake through the rhizosphere. It could be explained by the presence of mucilage deposits between the soil particles and the root surface, as recently proposed by Benard et al. (2018).

Conclusions

A deeper look into rhizosphere properties and functioning is greatly promoted by a synergistic combination of 3D noninvasive imaging methods, such as NCT and MRI. We used this method combination to determine the water content by NCT and to combine it with relaxation times that are sensitive to the molecular surroundings of water in the pore space. For example, if two water-filled equal-sized pores, one of which contains a gel, are compared, NCT would not see any difference as MRI relaxation times change. Our data show that the rhizosphere of broad bean extends across a distance of about 1 mm from the root surface to the bulk soil. In this zone NCT images confirmed an increased water content corresponding in position and spatial extent to the zone of decreased relaxation times available by MRI relaxation time mapping. The decrease in relaxation time can have several reasons, but the combination with the NCT results reduced the number of possible scenarios and led to the conclusion that the rhizosphere consists of a pore space modified by an additional gel phase. This view is supported by the subsequent drying and rewetting scenario on the same plant. The zone of decreased water content from NCT images corresponds exactly to the zone of reduced T_1 under previously saturated conditions. Quasi-simultaneous T_2 weighted MRI images confirm the persistence of this dry zone over 12 h. In parallel, we observed root water uptake through this dry zone that becomes manifest as a higher signal inside the root accompanied by decreased intensity in the bulk soil.

Our study has shown the potential of the combination of spatially resolved relaxation time mapping with high-resolution water content imaging by NCT. While the rhizosphere of broad bean in this example has only a small extent, the method is also suitable for investigations of rhizospheres with larger dimensions in the range of several millimeters to centimeters. Relaxation time mapping at 1.5 T especially offers the opportunity to monitor mucilage exudation into the rhizosphere or biofilm development in a time series. Because MRI delivers 3D datasets, spatial patterns can be monitored, too, i.e., along single roots but also throughout the entire root system. Such data could be the basis for statistical analysis in terms of correlation maps and the dependence on root segment age. Plants with a very fine root system below 0.1 mm and soils with higher amount of paramagnetic or even ferromagnetic impurities are challenging. Such material will require other MRI pulse sequences with ultrashort detection time.

Acknowledgments

We thank N. Rudolph-Mohr and P. Biró, Institute of Environmental Science and Geography, University Potsdam, Potsdam, Germany, as well as P. Vontobel and J. Hovind, PSI, Switzerland, for assistance with NCT measurements. We owe another thanks to J. Perlo and E. Danieli, Magritek Germany, Aachen, for the construction of the magnet and help with the pulse sequences; J. Neumann, ZEA-2, Research Center Jülich, for the construction of the vibration-damped trolley; and D. van Dusschoten, IBG-2, Research Center Jülich, for maintenance of the Varian MRI scanner. Financial support was granted by the German Research Foundation (DFG OS351/3-1 and HA6146/3-1, TR32).

References

Barrie, P.J. 2000. Characterization of porous media using NMR methods. Annu. Rep. NMR Spectrosc. 41:265–316. doi:10.1016/S0066-4103(00)41011-2

Belton, P.S. 1997. NMR and the mobility of water in polysaccharide gels. Int. J. Biol. Macromol. 21:81–88. doi:10.1016/S0141-8130(97)00045-7

Benard, P., M. Zarebanadkouki, C. Hedwig, M. Holz, M.A. Ahmed, and A. Carminati. 2018. Pore-scale distribution of mucilage affecting water repellency in the rhizosphere. Vadose Zone J. 17:170013. doi:10.2136/vzj2017.01.0013

Bertasa, M., T. Poli, C. Riedo, V. Di Tullio, D. Capitani, N. Proietti, et al. 2018. A study of non-bounded/bounded water and water mobility in different agar gels. Microchem. J. 139:306–314. doi:10.1016/j.microc.2018.03.016

Blümich, B. 2000. NMR imaging of materials. Clarendon Press, Oxford, UK.

Brax, M., C. Buchmann, and G. Schaumann. 2017. Biohydrogel induced soil–water interactions: How to untangle the gel effect? A review. J. Plant Nutr. Soil Sci. 180:121–141. doi:10.1002/jpln.201600453

Brax, M., C. Buchmann, and G.E. Schaumann. 2018. Effect of mucilage on water properties in the rhizosphere monitored by ^{1}H-NMR relaxometry. Microporous Mesoporous Mater. 269:47–50. doi:10.1016/j.micromeso.2017.07.044

Brownstein, K.R., and C.E. Tarr. 1977. Spin-lattice relaxation in a system governed by diffusion. J. Magn. Reson. 26:17–24.

Brownstein, K.R., and C.E. Tarr. 1979. Importance of classical diffusion in NMR studies of water in biological cells. Phys. Rev. A 19:2446–2453. doi:10.1103/PhysRevA.19.2446

Buchmann, C., and G. Schaumann. 2017. Effect of water entrapment by a hydrogel on the microstructural stability of artificial soils with various clay content. Plant Soil 414:181–198. doi:10.1007/s11104-016-3110-z

Callaghan, P.T. 1990. Principles of nuclear magnetic resonance microscopy. Oxford Univ. Press, Oxford, UK.

Carminati, A., A. Moradi, D. Vetterlein, P. Vontobel, E. Lehmann, U. Weller, et al. 2010. Dynamics of soil water content in the rhizosphere. Plant Soil 332:163–176. doi:10.1007/s11104-010-0283-8

Carminati, A., and D. Vetterlein. 2013. Plasticity of rhizosphere hydraulic properties as a key for efficient utilization of scarce resources. Ann. Bot. 112:277–290. doi:10.1093/aob/mcs262

Codd, S.L., S.J. Vogt, J.A. Hornemann, A.J. Phillips, J.E. Maneval, K.R. Romanenko, et al. 2011. NMR relaxation measurements of biofouling in model and geological porous media. Org. Geochem. 42:965–971. doi:10.1016/j.orggeochem.2011.03.014

Couchat, P., P. Moutonnet, M. Houelle, and D. Picard. 1980. In situ study of corn seedling root and shoot growth by neutron radiography. Agron. J. 72:321–324. doi:10.2134/agronj1980.00021962007200020017x

Danieli, E., K. Berdel, J. Perlo, W. Michaeli, U. Masberg, B. Bluemich, and F. Casanova. 2010. Determining object boundaries from MR images with sub-pixel resolution: Towards in-line inspection with a mobile tomograph. J. Magn. Reson. 207:53–58. doi:10.1016/j.jmr.2010.08.004

Duschl, M., A. Pohlmeier, T. Brox, P. Galvosas, and H. Vereecken. 2016. Effect of magnetic pore surface coating on the NMR relaxation and diffusion signal in quartz sand. Magn. Reson. Chem. 54:975–984. doi:10.1002/mrc.4486

Esser, H.G., A. Carminati, P. Vontobel, E.H. Lehmann, and S.E. Oswald. 2010. Neutron radiography and tomography of water distribution in the root zone. J. Plant Nutr. Soil Sci. 173:757–764. doi:10.1002/jpln.200900188

Furukawa, J., T.M. Nakanishi, and H. Matsubayashi. 1999. Neutron radiography of a root growing in soil with vanadium. Nucl. Instrum. Methods Phys. Res., Sect. A 424:116–121. doi:10.1016/S0168-9002(98)01279-0

Gardner, W.R. 1960. Dynamic aspects of water availability to plants. Soil Sci. 89:63–73. doi:10.1097/00010694-196002000-00001

Gregory, P.J. 2006. Roots, rhizosphere and soil: The route to a better understanding of soil science? Eur. J. Soil Sci. 57:2–12. doi:10.1111/j.1365-2389.2005.00778.x

Gregory, P.J., and P. Hinsinger. 1999. New approaches to studying chemical and physical changes in the rhizosphere: An overview. Plant Soil 211:1–9. doi:10.1023/A:1004547401951

Haber-Pohlmeier, S., S. Stapf, and A. Pohlmeier. 2014. NMR fast field cycling relaxometry of unsaturated soils. Appl. Magn. Reson. 45:1099–1115. doi:10.1007/s00723-014-0599-2

Haber-Pohlmeier, S., C. Tötzke, S. Oswald, B. Blümich, and A. Pohlmeier. 2018. Imaging of root zone processes using MRI T_1 mapping. Microporous Mesoporous Mater. 269:43–46. doi:10.1016/j.micromeso.2017.10.046

Haber-Pohlmeier, S., J. Vanderborght, and A. Pohlmeier. 2017. Quantitative mapping of solute accumulation in a soil–root system by magnetic resonance imaging. Water Resour. Res. 53:7469–7480. doi:10.1002/2017WR020832

Hinsinger, P., A.G. Bengough, D. Vetterlein, and I.M. Young. 2009. Rhizosphere: Biophysics, biogeochemistry and ecological relevance. Plant Soil 321:117–152. doi:10.1007/s11104-008-9885-9

Kardjilov, N., A. Hilger, I. Manke, A. Griesche, and J. Banhart. 2015. Imaging with cold neutrons at the CONRAD-2 facility. Phys. Procedia 69:60–66. doi:10.1016/j.phpro.2015.07.008

Keyes, S.D., K.R. Daly, N.J. Gostling, D.L. Jones, P. Talboys, B.R. Pinzer, et al. 2013. High resolution synchrotron imaging of wheat root hairs growing in soil and image based modelling of phosphate uptake. New Phytol. 198:1023–1029. doi:10.1111/nph.12294

Kimmich, R. 2012. Principles of soft matter dynamics. Springer, Dordrecht, the Netherlands. doi:10.1007/978-94-007-5536-9

Kleinberg, R.L., W.E. Kenyon, and P.P. Mitra. 1994. Mechanism of NMR relaxation of fluids in rocks. J. Magn. Reson., Ser. A 108:206–214. doi:10.1006/jmra.1994.1112

Lehmann, E., P. Vontobel, and L. Witzel. 2001. Properties of the radiography facility NEUTRA at SINQ and its potential for use as European reference facility. Nondestr. Test. Eval. 16:191–202. doi:10.1080/10589750108953075

MacFall, J.S., G.A. Johnson, and P.J. Kramer. 1990. Observation of a water depletion region surrounding loblolly pine roots by magnetic resonance imaging. Proc. Natl. Acad. Sci. 87:1203–1207. doi:10.1073/pnas.87.3.1203

Matsushima, U., W.B. Herppich, N. Kardjilov, W. Graf, A. Hilger, and I. Manke. 2009. Estimation of water flow velocity in small plants using cold neutron imaging with D_2O tracer. Nucl. Instrum. Methods Phys. Res., Sect. A 605:146–149. doi:10.1016/j.nima.2009.01.187

McRobbie, D.W., E.A. Moore, M.J. Gaves, and M.R. Prince. 2007. MRI from picture to proton. Cambridge Univ. Press, Cambridge, UK.

Metzner, R., A. Eggert, D. van Dusschoten, D. Pflugfelder, S. Gerth, U. Schurr, et al. 2015. Direct comparison of MRI and X-ray CT technologies for 3D imaging of root systems in soil: Potential and challenges for root trait quantification. Plant Methods 11:17. doi:10.1186/s13007-015-0060-z

Moradi, A.B., A. Carminati, D. Vetterlein, P. Vontobel, E. Lehmann, U. Weller, et al. 2011. Three-dimensional visualization and quantification of water content in the rhizosphere. New Phytol. 192:653–663. doi:10.1111/j.1469-8137.2011.03826.x

Nishiyama, H. 2005. Water gradient profiles at bean plant roots determined by neutron beam analysis. J. Radioanal. Nucl. Chem. 264:313–317. doi:10.1007/s10967-005-0713-x

Oswald, S.E., C. Tötzke, S. Haber-Pohlmeier, A. Pohlmeier, A. Kästner, and E. Lehmann. 2015. Combining neutron and magnetic resonance imaging to study the root–soil interface. Phys. Procedia 69:237–243. doi:10.1016/j.phpro.2015.07.033

Peth, S. 2010. Applications of microtomography in soils and sediments. Dev. Soil Sci. 34:73–191. doi:10.1016/S0166-2481(10)34003-7

Segal, E., T. Kushnir, Y. Mualem, and U. Shani. 2008. Microsensing of water dynamics and root distributions in sandy soils. Vadose Zone J. 7:1018–1026. doi:10.2136/vzj2007.0121

Tötzke, C., N. Kardjilov, I. Manke, and S.E. Oswald. 2017. Capturing 3D water flow in rooted soil by ultra-fast neutron tomography. Sci. Rep. 7:6192. doi:10.1038/s41598-017-06046-w

Tumlinson, L.G., H.Y. Liu, W.K. Silk, and J.W. Hopmans. 2008. Thermal neutron computed tomography of soil water and plant roots. Soil Sci. Soc. Am. J. 72:1234–1242. doi:10.2136/sssaj2007.0302

van Veelen, A., M.C. Tourell, N. Koebernick, G. Pileio, and T. Roose. 2018. Correlative visualization of root mucilage degradation using X-ray CT and MRI. Front. Environ. Sci. 6:32. doi:10.3389/fenvs.2018.00032

Vetterlein, D., T. Kuehn, K. Kaiser, and R. Jahn. 2013. Illite transformation and potassium release upon changes in composition of the rhizosphere soil solution. Plant Soil 371:267–279. doi:10.1007/s11104-013-1680-6

Whalley, W.R., B. Riseley, P.B. Leeds-Harrison, N.R.A. Bird, P.K. Leech, and W.P. Adderley. 2005. Structural differences between bulk and rhizosphere soil. Eur. J. Soil Sci. 56:353–360. doi:10.1111/j.1365-2389.2004.00670.x

Young, I.M. 1995. Variation in moisture contents between bulk soil and the rhizosphere of wheat. New Phytol. 130:135–139. doi:10.1111/j.1469-8137.1995.tb01823.x